

A numerical model to simulate the transient frictional viscoelastic sliding contact

Dongze WANG*, Gregory de BOER, Anne NEVILLE, Ali GHANBARZADEH

School of Mechanical Engineering, University of Leeds, Leeds LS2 9JT, UK

Received: 07 February 2023 / Revised: 01 May 2023 / Accepted: 22 May 2023

© The author(s) 2023.

Abstract: Sliding motion has always been one of the major concerns when it comes to the analysis of viscoelastic contact problems. A new model simulating the transient sliding contact of smooth viscoelastic surfaces is developed in this paper. By taking the dry contact friction and the coupling between shear tractions and normal pressure into account, the effect of the early partial slip period, which is often neglected in the study of viscoelastic sliding contact problems, is investigated numerically. Compared with solutions based on the frictionless assumption, the steady-state pressure profile is found to be slightly different under the effect of the partial slip regime, including a lower peak pressure and the shift of the contacting region in the direction opposite to the sliding motion. Furthermore, the time required for the viscoelastic contact to reach its steady state is delayed owing to the partial slip period preceding the global sliding motion.

Keywords: contact mechanics; frictional sliding; viscoelasticity; viscoelastic friction

1 Introduction

Beyond natural selection, viscoelastic materials have been universally applied in practice owing to their numerous advantages such as low friction, slight rubbing noise, light weight, dimensional stability and inexpensive cost. A more efficient design of engineering products involving viscoelasticity requires a clear understanding of the relevant interfacial mechanical system, which is determined by the viscoelastic deformation, viscoelastic dissipation, frictional temperature rise, time-dependent material property and lubrication condition. In the meantime, the prevailing relative motion between the contacting bodies including sliding and rolling can be critical during the viscoelastic contact analysis. Typical examples of such a scenario are the tire-road contact [1] for vehicles, the cutting of soft tissues with scalpels during operations [2], the contact between underlying bones and articular cartilages in human bodies [3], the interaction between the polymer liner

component and metal femoral component observed for hip implants [4] and the delightful mouthfeel when tasting chocolate [5].

In practice, a wide range of length scales and time scales is required to characterize wavelengths of rough surfaces and relaxation times of viscoelastic materials, respectively. Meanwhile, the time-dependent constitutive laws make it more challenging to address real-life viscoelastic sliding and rolling contact problems theoretically and experimentally [6]. Nevertheless, a number of early attempts have been made by different researchers. Hunter [7] studied the two-dimensional (2D) frictionless problem of a rigid cylinder rolling over a viscoelastic half-space. This steady-state solution was later extended by Panek and Kaller [8] to 3D problems by adopting an approximation on the basis of elastic line integral theory. The contact friction was taken into account in the line contact problem by Goriacheva [9]. However, the pressure solution was not affected by the dry contact friction (shear traction) as the two contacting viscoelastic

* Corresponding author: Dongze WANG, E-mail: mn17d2w@leeds.ac.uk

bodies were assumed to exhibit the same mechanical properties (e.g., no coupling between shear tractions and pressures). Apart from these plane strain problems, Aleksandrov et al. [10] simulated the frictionless sliding contact between a smooth sphere and a viscoelastic half-space. The application of these approaches is limited to ideal viscoelastic materials with one relaxation time. Based on the assumption that the viscoelastic material stiffens when the rolling speed increases (e.g., higher frequency) while the pressure distribution remains of a Hertzian type, a novel analytical theory was proposed by Persson to solve the rolling contact of a rigid cylinder or a sphere over a flat viscoelastic substrate [11]. The rolling friction coefficient can be estimated reasonably by the theory of Persson. However, the information on pressure distribution especially its non-Hertzian profile in a force-driven problem is not available within the framework of this theory.

To overcome the drawbacks of these analytical solutions, great efforts have been made in the past decades in developing numerical models that can take into account any viscoelastic material and any geometry of contacting bodies [12]. One of the most common modelling tools, e.g., the finite element method (FEM), was frequently employed in early attempts to simulate viscoelastic rolling and sliding contact problems based on Lagrangian formulations [13–18]. However, the computational cost can be relatively high for models based on FEM when addressing rough contact problems since they require an extremely fine mesh to capture complex surface irregularities. In this case, the fast Fourier transform (FFT) assisted boundary element method (BEM), also referred to as the semi-analytical method (SAM), is widely applied as an alternative. Carbone and Putignano [19] developed a BEM-based model to generate steady-state solutions to rough sliding or rolling contact problems [20], where the involved viscoelastic material can either exist as the form of a half-space [21] or a layer [22–24] with finite thickness. Recently, Zhao et al. [25] adopted a novel formulation, which relates the surface deformation to contact tractions, to simulate the frictionless sliding or rolling contact of viscoelastic surfaces. They claimed that the new equation helps to improve the computational efficiency of their BEM-based

model using computational techniques including multi-grid and multilevel multi-integration (MLMI) methods [26, 27].

Regarding the transient viscoelastic analysis using BEM, the frictionless rolling contact of a rigid smooth indenter against a flat viscoelastic half-space was simulated by Koumi et al. [28], where the material inhomogeneity is considered. The frictionless contact of an incompressible viscoelastic semi-infinite body rolling on a rough rigid surface was analyzed by Bugnicourt et al. [29]. Wallace et al. [30] proposed a model which provides transient analysis of frictionless rolling and sliding viscoelastic problems, in which the involved viscoelastic layer and substrate can exhibit distinct properties. The effects of imperfect bonding between layer and substrate on the transient as well as steady-state frictionless viscoelastic sliding contact problems were recently investigated by Zhang et al. [31].

It is noted that considering the transient response is computationally demanding as all the time scales that describe the behaviour of viscoelastic materials need to be tracked. Additionally, the numerical time interval must be sufficiently small to capture the occurrence of sudden events. This explains why several researchers focused on the steady-state response of the contact problems instead of the transient response by making use of the constant complex modulus of viscoelastic materials [19–22, 31]. Such analysis shall work well for frictionless viscoelastic sliding or rolling contact problems as precise knowledge of the tangential field is not needed. However, during the transient part of frictional sliding, the contact area can be separated into stick and slip regions when the transient tangential load is not enough to induce gross sliding. This separation may play an important role in determining the later gross sliding behaviour. There exists some literature reporting the effects of dry contact friction in the sliding contact of viscoelastic surfaces such as the work of Goryacheva et al. [32, 33]. To date, the effects of friction, especially the evolution from partial slip to gross sliding in transient viscoelastic sliding contact problems, are barely investigated numerically [12], which is the subject of the current study. Furthermore, few reports have elucidated the effect of surface roughness on the transient sliding of viscoelastic materials in the presence of contact friction.

A frictional sliding contact model for viscoelastic materials is developed in this study, where transient contact solutions are available. The steady-state solution can be achieved by extending the simulation time. The modelling starts from the quasi-static state to the dynamic state, where the complete transition from partial slip to gross sliding and the coupling effects between shear traction and pressure are considered. A novel strategy to simulate the surface movement during the global slip stage is proposed, which is convenient to be implemented compared with other approaches in Refs. [30, 34]. The effects of the partial slip period on the later sliding contact solutions are investigated with the model, including the role of the shear traction and the time when the partial slip ends (before or after the time when the material property becomes steady).

2 Theory and algorithm description

To explain how the model of frictional viscoelastic sliding contact is developed, some basic terminology and relationships commonly used to describe the behaviour of viscoelastic materials are first presented in this section.

2.1 Theory of linear viscoelasticity and friction

Among viscoelastic materials, those exhibiting a linear relationship between stress and strain at any time are known as linear viscoelastic materials. The materials simulated in the current study are assumed to behave linearly following the infinitesimal strain theory. As viscoelastic materials are usually soft, they can hardly experience plastic deformation. Therefore, the plastic contact is neglected in the following modelling work. In addition, all the analyses presented here are under isothermal conditions. In other words, the temperature effects on the mechanical behaviour of materials are not considered during the simulation.

Following the theory of linear viscoelasticity, the responses of stress (denoted as vector σ) to successive strain (denoted as vector ε) stimuli are cumulative and vice versa, which can be described as Eqs. (1) and (2) by using the Boltzmann hereditary integral:

$$\sigma(t) = \int_0^t \psi(t-t') \frac{d\varepsilon(t')}{dt'} dt' \quad (1)$$

$$\varepsilon(t) = \int_0^t \phi(t-t') \frac{d\sigma(t')}{dt'} dt' \quad (2)$$

where $\psi(t)$ and $\phi(t)$ are known as the relaxation modulus function and creep compliance function respectively.

Different from an ideal elastic contact material where the compliance and modulus are mutually reciprocal, there exists the essential mathematical relationship in Eq. (3) between the two material properties for linear viscoelastic materials in the Laplace transform domain:

$$\bar{\phi}(s)\bar{\psi}(s) = \frac{1}{s^2} \quad (3)$$

where s is the variable in the Laplace transform domain ($s = a + jb$).

The time-dependent mechanical response of linear viscoelastic materials can be characterised in a discretised form by building rheological models. By arranging several springs and dashpots in series or parallel, different rheological models can be constructed. Among them, the Generalized Weichert model shown in Fig. 1 is usually employed to characterise the complicated response of realistic materials such as polymethyl methacrylate (PMMA) [35]. With the Generalized Weichert model, the relaxation modulus function of any linear viscoelastic material can be expressed appropriately by fitting the experimental data collected from the conducted relaxation test to Eq. (4) (Prony series) and adjusting the parameters:

$$\psi(t) = G_0 + \sum_{i=1}^n G_i \exp\left(-\frac{t}{\tau_i}\right) \quad (4)$$

where the subscript “ i ” is the index notation of the spring and dashpot in series ($i = 1 \dots n$) as shown in Fig. 1. G is the spring modulus and τ is the relaxation time ($\tau_i = \eta_i / G_i$) with η denoting the viscosity of the dashpot.

Once the relaxation modulus function is available, the corresponding creep compliance function can be easily determined as well by utilizing their mathematical relationship in the Laplace transform

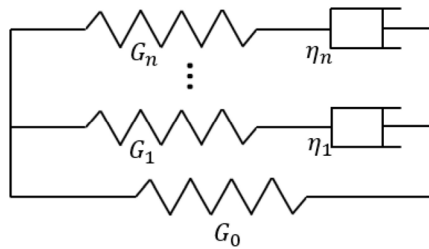


Fig. 1 Structure of the Generalized Weichert model: G is spring modulus and η is viscosity of dashpot.

domain (3). If the material is characterized by one relaxation time in this case (only one spring in series with one dashpot), such a three-element model is known as the Zener model or standard linear solid model. Zener models are commonly employed to build fictitious viscoelastic materials for the numerical study of the properties of different viscoelastic materials [30, 36, 37].

To avoid confusion about concepts of friction in the following modelling work, different friction laws commonly employed in contact analysis are stated here in advance. The first is the Amontons–Coulomb friction law (short for Coulomb friction law hereinafter). It describes the macroscale phenomenon that when a solid is under sliding, it opposes a tangential force proportional to the normal force. It is widely applied in many studies due to its simplicity and versatility [32, 33, 36, 38, 39]. If this approximation is not satisfactory enough to characterise the contact phenomena occurring at different scales, it is always easy to modify the law to make the friction coefficient dependent on different parameters such as pressure and velocity. The second is the constant shear stress friction law, which claims that friction is affected by contact conditions. This law is usually employed to characterise the contact phenomena occurring on the microscale, where the role of van der Waals bonds and physisorption becomes essential. Besides, the surface roughness tends to affect the friction force in this case. Apart from these two laws, the viscoelastic losses that happened in the bulk of a viscoelastic material can result in some friction force. The apparent friction coefficient analysed in the frictionless viscoelastic sliding or rolling contact modelling work is related to the friction derived from the viscoelasticity of materials.

When it comes to the viscoelastic sliding contact analysis, friction is always deduced from viscoelastic losses such as these frictionless simulation studies [7, 19, 28–31]. The word ‘frictionless’ in these works means that the dry contact friction is not included in the sliding or rolling analysis. However, the frictional force derived from the hysteresis losses in the deformation cycles of viscoelastic materials is taken into account. The reason behind such practice is relevant to the intrinsic property of some specific polymers. It is known that elastomers are incompressible. For the problem of an incompressible half-space sliding on a rigid surface, there exists no coupling between the normal pressure and shear tractions. A good representation of this type of frequently investigated problem is the rubber tyre sliding on the hard road surface on the mesoscale, as investigated by Bugnicourt et al. [29]. As the normal and tangential contact problems are independent of each other, the simplest way to simulate the sliding or rolling contact problems of viscoelastic materials is to neglect shear tractions in the lateral direction, together with their related coupling effects affecting the pressure profile, and to quantify the friction force exclusively derived from the viscoelastic losses. However, the case where uncoupled conditions can be applied is not ubiquitous. When addressing the common material combination for engineering products such as the knee or hip prosthesis (usually a hard metal against a soft and compressible polymer), the inclusion of the coupling effect seems inevitable. Furthermore, evidence can be found that as the modulus of viscoelastic materials changes with time, so does the Poisson’s ratio [40, 41]. Because the latter quantity governs the coupling between normal and tangential tractions, a fully coupled model, which provides information on both normal and tangential fields in viscoelastic contact problems, is worth studying for fine precision engineering applications. It is noteworthy that the applications of first and third friction laws do not conflict with each other, although frictional forces are derived from different media. For example, in the experimental study on the frictional behaviour of sliding viscoelastic materials by Carbone and Putignano [19], the Coulomb friction coefficient (characterising dry contact friction) and

apparent friction coefficient (characterising viscoelastic losses) were applied in an additive manner (e.g., the total friction force is the summation of the dry contact friction and viscoelastic friction).

2.2 Problem formulation and algorithm development

The 3D problem of a rigid sphere sliding on a compressible viscoelastic half-space with contact friction is illustrated in Fig. 2. The formulation for the frictional sliding contact problem can be divided into two parts including the partial slip and fully sliding problems.

To discretize the problem based on BEM, the potential contact region between the two contacting surfaces is meshed into equally spaced rectangular elements with the size of $\Delta_1 \times \Delta_2$ and number of $N_1 \times N_2$ in x and y directions respectively. Temporal discretization is necessary to model transient viscoelastic contact problems. The simulation time T is discretized into N_t time steps with a time interval that is uniform and short enough that the element pressure can be assumed to be constant for each time interval.

Coulomb friction law is employed here to determine the dry contact friction and to identify the stick or slip state of each surface node before gross sliding. A constant coefficient of friction μ_f is assumed for the sake of simplicity. To further facilitate the determination of contact tractions, semi-coupled conditions (coupling between pressure p and the shear traction in x direction q_x) are implemented during the simulation.

The surface movement after the partial slip period needs to be included in the dynamic sliding problem.

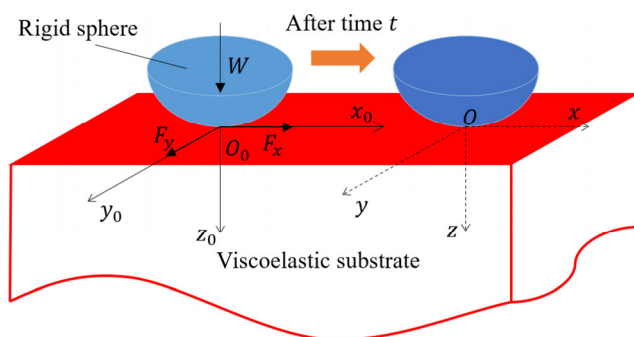


Fig. 2 Geometrical description of the frictional contact of a rigid sphere against a viscoelastic half-space under input loads (the sphere slides with a constant velocity v once the contact reaches the gross sliding state).

This can be achieved by changing the coordinates of the contact problem correspondingly with the sliding motion. The Cartesian coordinate system used during the simulation process either maintains or keeps being updated according to the sliding state of the surface being experienced. During the partial slip period, a fixed coordinate system $R_0(O_0, X_0, Y_0, Z_0)$, which corresponds to the initial contact set of axes at the initial simulation time ($t = 0$), is employed. Once the surfaces are in the gross sliding stage, the coordinate system $R(O, X, Y, Z)$ must follow the movement of the rigid sphere to search for the transient contact solutions in the updated contact fields. The contact conditions and equations are formulated in a new coordinate system, which is centred on the projection of the centre of the indenter on the flat half-space.

To assume that the sliding velocity of viscoelastic surfaces remains constant after reaching the fully slip state, by relating the sliding velocity (v) to the pixel width (Δ_1, Δ_2), the coordinates of the rigid sphere are translated by one mesh element in the sliding direction at each time step. This approach can avoid updating the surface geometry by the interpolation of surfaces according to the slip distance at each time step [31, 34], which could be time-consuming and also undermine the accuracy of simulation results.

However, since the size of the computational domain is intended to remain unchanged during the simulation, information on past pressure history might be partially lost due to the update (movement) of the system coordinate. As the size of the mesh element is affected by the constant sliding velocity, the number of nodes must be large enough that the computational domain can characterize the creep of the contacting area when the velocity is relatively low. A considerably large number of nodes (e.g., 512×512 or $1,024 \times 1,024$) is needed to keep the whole past pressure history available when the total simulation time is long and the time step is extremely small. Therefore, a compromise might need to be made between computational efficiency and accuracy when this approach to updating surface movement is adopted. A detailed discussion on the effect of the lost past pressure history is given in Section 3.

To apply the elastic–viscoelastic correspondence principle, the surface displacement at any position

caused by the contact tractions at any time can be determined as Eq. (5):

$$u_{\alpha\beta}(i, j, k) = \sum_{n=1}^{N_t} \sum_{l=1}^{N_1} \sum_{m=1}^{N_2} IC_{\alpha\beta}(i-l, j-m, k-n)(t_\gamma(l, m, n) - t_\gamma(l, m, n-1)) \tag{5}$$

where $u_{\alpha\beta}$ is the displacement in $\alpha(\alpha = x, y, z)$ direction caused by the traction in $\beta(\beta = x, y, z)$ direction and t_γ is the contact traction in the $\gamma(\gamma = x, y, z)$ direction. $IC_{\alpha\beta}(i-l, j-m, k-n)$ is known as the viscoelastic influence coefficient characterizing the displacement in α direction observed after k time steps in the node (i, j) of the spatial mesh under the effect of uniform traction in the β direction which acts on the node (l, m) in the n -th time step after the reference time, with $n \leq k$ ($i = 1 \dots N_1, j = 1 \dots N_2, \text{ and } k = 1 \dots N_t$). For a detailed description of how to determine the influence coefficient based on Boussinesq solutions [42] using the correspondence principle, readers can refer to the work by Wang et al. [36].

In the current study, only the tangential problem in the x direction is considered. The nodal displacements of the viscoelastic half-space induced by an arbitrary history of nodal tractions under semi-coupled conditions can then be expressed as Eq. (6):

$$\begin{bmatrix} u_x \\ u_z \end{bmatrix} = \sum_{n=1}^{N_t} \sum_{l=1}^{N_1} \sum_{m=1}^{N_2} \begin{bmatrix} IC_{xx}(i-l, j-m, k-n) & IC_{xz}(i-l, j-m, k-n) \\ IC_{zx}(i-l, j-m, k-n) & IC_{zz}(i-l, j-m, k-n) \end{bmatrix} \begin{bmatrix} q_x(l, m, n) - q_x(l, m, n-1) \\ p_z(l, m, n) - p_z(l, m, n-1) \end{bmatrix} \tag{6}$$

where discrete convolution fast Fourier transform (DC-FFT) is applied to accelerate the convolution operations.

A quasi-static process is assumed to avoid the problem of dissipative friction and its irreversibility related to the load-path dependency when addressing the partial slip problem. As mentioned before, the Poisson’s ratio of a realistic viscoelastic material employed in practice is usually time-dependent [40, 41], but it is assumed to be constant here for simplicity.

The frictional sliding contact problem can be solved by searching for solutions that can satisfy the following boundary conditions:

(1) Load balance: The sum of the pressure within the

contact area should always be equal to the specified normal load at any time step. This can be expressed as Eq. (7):

$$W(t) = \Delta \sum_{(i,j) \in I_c(k)} p(i, j, k) \tag{7}$$

where W denotes the applied normal load, Δ denotes the area of an individual element ($\Delta_1 \times \Delta_2$), and I_c denotes the time-varying contact region.

(2) The surface displacement of the contacting surfaces should meet the geometrical condition in Eq. (8) in the normal direction:

$$h(i, j, k) = h_i(i, j) + u_z(i, j, k) - \delta_z(k), (i, j) \in I_p \tag{8}$$

where h_i is the gap between undeformed surfaces, h is the surface gap after loading, δ_z is the normal rigid body displacement, and I_p denotes the computational domain.

In the lateral direction, the condition in Eq. (9) must be satisfied:

$$s_x(i, j, k) = u_x(i, j, k) - \delta_x(k), (i, j) \in I_c(k) \tag{9}$$

where s_x denotes the slip distance in the x direction and δ_x denotes the rigid body displacement in the x direction.

(3) The following complementary condition must be met to obtain valid contact solutions:

The Kuhn–Tucker complementary conditions should be satisfied in the normal direction at any time point, which also implies that there exists no surface adhesion and the simulated surfaces are impenetrable:

$$\begin{aligned} p(i, j, k) > 0 \ \& \ h(i, j, k) = 0, (i, j) \in I_c(k); \\ p(i, j, k) = 0 \ \& \ h(i, j) > 0, (i, j) \in I_p - I_c(k) \end{aligned} \tag{10}$$

where $I_p - I_c$ denotes the non-contacting region within the computational domain.

During the partial slip period, the stick or slip state of each surface node within the contacting region I_c can be distinguished by the boundary conditions in Eq. (11) in the tangential direction:

$$\begin{aligned} |q_x(i, j, k)| < \mu_f p(i, j, k), s_x(i, j, k) = 0, (i, j) \in I_{st}(k), \\ q_x(i, j, k) \cdot s_x(i, j, k) < 0, (i, j) \in I_c(k) - I_{st}(k), \\ |q_x(i, j, k)| = \mu p(i, j, k), s_x(i, j, k) \neq 0, (i, j) \in I_c(k) - I_{st}(k) \end{aligned} \tag{11}$$

where I_{st} denotes the stick region and $I_c - I_{st}$ denotes the slip region.

Once the surface starts to slide globally, the shear traction q_x is always equal to the local friction expressed as Eq. (12):

$$q_x(i, j, k) = \mu_f \cdot p(i, j, k), (i, j) \in I_c(k) \quad (12)$$

The algorithm for the frictional sliding contact problems is shown in Fig. 3, which can be separated into two sections including the partial slip and fully sliding solvers. As illustrated, the contact solutions to the semi-coupled partial slip problem keep being searched until the ratio of the stick region to the contacting area (short for stick ratio hereinafter) vanishes. A detailed description of the partial slip solver can be found in our previous work on the partial slip modelling of viscoelastic surfaces [36]. Once the surface starts to slide, only the normal contact problem needs to be addressed as the shear traction is always equal to the local friction. During the sliding phase, the process to search for solutions to the frictional sliding problem is similar to that for a frictionless problem. The difference is the time when the coordinate system of the contact field needs to be updated (i.e., the time when the partial slip ends). This is determined by the past pressure history affected by the coupling effects with shear traction, and the extra normal displacement derived from the shear traction.

It is of note that the reason why fully coupled conditions between shear tractions and pressures are not applied is relevant to the way the algorithm

produces contact solutions to partial slip solutions. When normal and tangential problems are fully coupled, the state of gross sliding is identified by checking if the algorithm of the partial slip solver fails to separate the stick and slip regions and outputs NaN (not a number) results in MATLAB. Therefore, the exact contact tractions are not accessible when surfaces are in the sliding state under fully coupled conditions.

3 Model validation

Since the coupled partial slip aspect of the model has been validated and described in detail in our previous work [36, 39], only the validation work of its fully slip field is shown in this section. By simulating a frictionless sliding contact problem of a rigid sphere against a viscoelastic half-space, the sliding aspect is validated by comparing the simulation results from the degenerated forms of our developed model with the corresponding results reported by Koumi et al. [28]. The contact input specified during the simulation is given in Table 1. To capture the creep phenomena of the contacting area under different sliding speeds, the computational domain is set to be $-3.84a_0 \times 3.84a_0$ for the case with the highest speed ($v = 1.2a_0 / \tau$) while a smaller computational domain ($-2.56a_0 \times 2.56a_0$) is employed for the cases with the lowest and medium speeds ($v = 0.4a_0 / \tau$ and $v = 0.8a_0 / \tau$ respectively). The computational domain is discretized by 256×256 nodes.

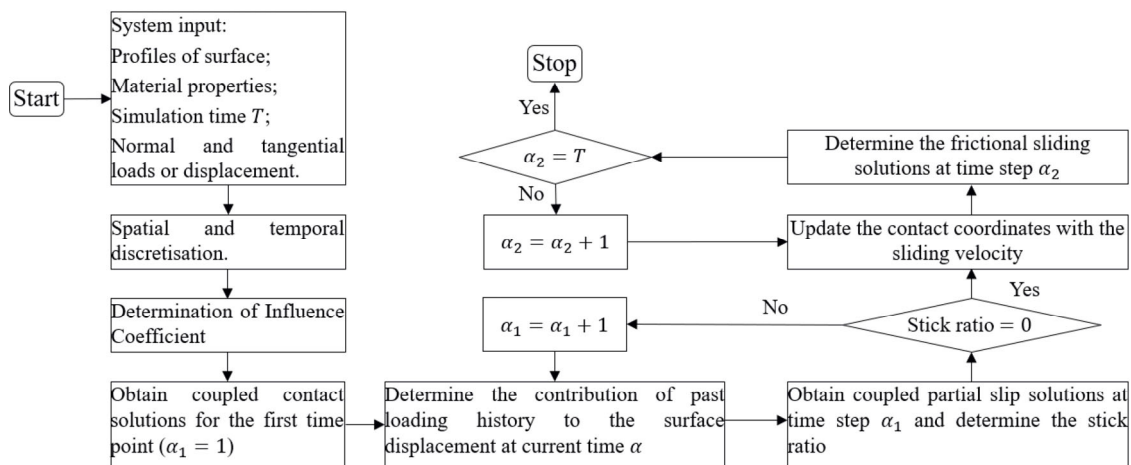


Fig. 3 Flow chart of the algorithm for the frictional viscoelastic problem.

Table 1 Contact parameters employed in the validation test.

Parameter	Value	Description (unit)
W	1.48	Input indentation load (N)
R	10	Radius of the sphere (mm)
μ_∞	3.86	Initial shear modulus of material (MPa)
$\frac{\mu_\infty}{\mu_0}$	10	Ratio of retardation time to relaxation time (ratio of initial shear modulus to modulus after infinite time)
τ	0.01	Relaxation time of the viscoelastic material (s)
T	4τ	Total simulation time (s)
ν	0.3	Poisson's ratio of the viscoelastic material
a_0	588.7	Hertzian contacting radius for nondimensionalization (μm)
p_0	0.2067	Hertzian peak normal pressure for nondimensionalization (MPa)
v	$0.4a_0/\tau$ $0.8a_0/\tau$ $1.2a_0/\tau$	Constant frictionless sliding speed of the surface (normalized)

A Zener model is employed to characterize the mechanical response of the viscoelastic half-space, where the relaxation modulus and creep compliance are usually described in Eqs. (13) and (14):

$$\psi(t) = \mu_0 + (\mu_\infty - \mu_0) \exp\left(-\frac{t}{\frac{\mu_0}{\mu_\infty} \tau}\right) \quad (13)$$

$$\phi(t) = \frac{1}{\mu_\infty} + \frac{1}{\mu_1} \left(1 - \exp\left(-\frac{t}{\tau}\right)\right), \mu_1 = \frac{1}{\frac{1}{\mu_0} - \frac{1}{\mu_\infty}} \quad (14)$$

where μ_∞ is the initial shear modulus and μ_0 is the modulus after infinite time. It is noted that the parameter $\frac{\mu_\infty}{\mu_0}$, which is known as the ratio of retardation time to relaxation time, determines the rheological behaviour of viscoelastic material characterized by a Zener model [36].

The simulation results under the given contact inputs are normalized by the Hertzian solution based on the instantaneous modulus $\Psi(0)$ and the input load W . Since the pressure profile tends to become steady after the time of 2τ , transient pressure distributions at four different time points within the simulation of 2τ are plotted. As a fixed normal load is applied, the creep of contacting area with time can

be observed in Figs. 4(a)–4(c) for the three tests with different sliding velocities. Due to the resistance force arising from the viscoelasticity of the material during sliding, the pressure is distributed non-symmetrically. Compared with the pressure at the trailing edge of the contact area, that at the leading edge tends to be higher showing a sharp spike. Besides, the contact region shifts in the sliding direction with time even though the effects of shear stress on the pressure are neglected in the current frictionless tests. Meanwhile, the increase in the sliding velocity is found to cause an increase in the peak pressure, a decrease in the contacting area and a more pronounced contact shift phenomenon. One can see from Figs. 4(a)–4(c) that the back side of the contacting area becomes closer to the centre of the indenter when the sliding velocity increases.

To quantify the friction derived from viscoelastic loss, the apparent friction coefficient μ_{app} is usually determined. A time-dependent tangential force F_T can be induced by the hysteresis loss within a viscoelastic material, which can be calculated as Eq. (15):

$$F_T(t) = \int \int_{I_c(t)} \frac{\partial u_z(x, y, t)}{\partial x} p(x, y, t) dx dy \quad (15)$$

As a common practice, the finite difference method is used to calculate the factor $\frac{\partial u_z(x, y, t)}{\partial x}$, and the rectangle rule is applied to evaluate the integral for $F_T(t)$. The apparent friction coefficient μ_{app} can then be calculated as the ratio of the resulting tangential force F_T to the applied normal load W .

As shown in Fig. 4(d), for all the tests, the apparent friction coefficient tends to become steady when the simulation time reaches 3τ . This coefficient is affected by the sliding velocity such that a higher velocity leads to a higher apparent friction coefficient (more viscoelastic friction). It is noted that such a monotonic trend only holds for viscoelastic contacts with low or medium sliding velocity. When the sliding velocity is considerably high, the response of the apparent friction coefficient to the sliding velocity tends to be the opposite. A complete map showing the evolution of the apparent friction coefficient with the normalized sliding velocity, which is also known as the Deborah number, can be found in the steady viscoelastic contact analysis by Carbone and Putignano [19].

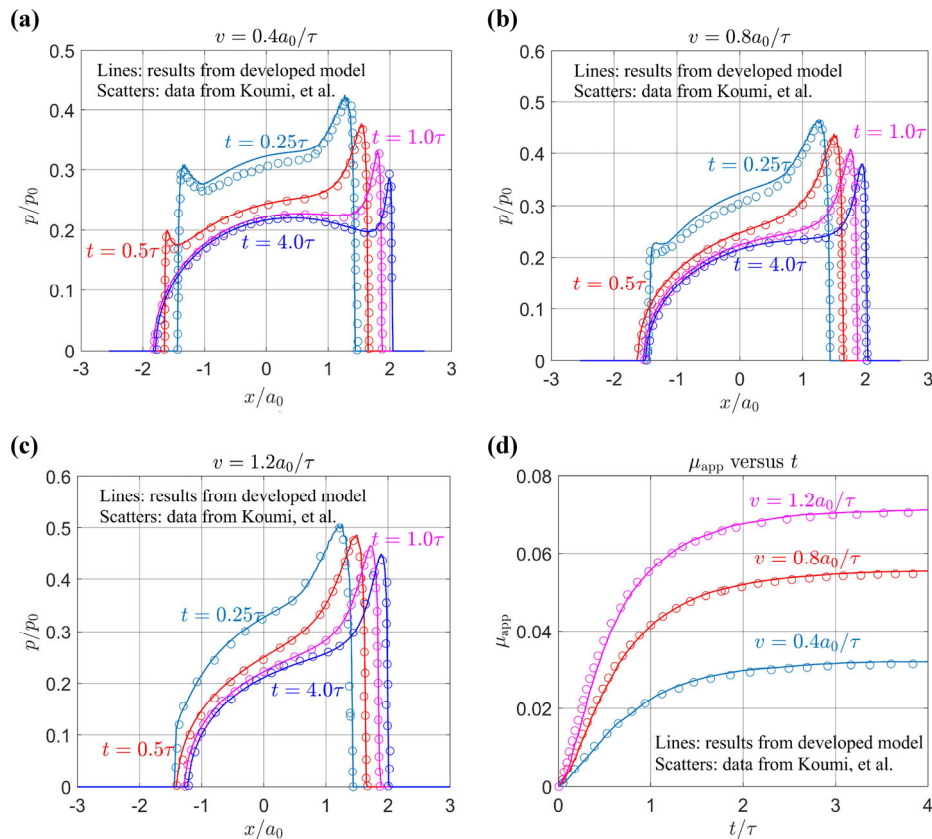


Fig. 4 Comparison of the simulation results from our model (solid lines) with the results from Koumi et al. [28]. Reproduced with permission from Ref. [28], © Elsevier B. V., 2023. (a)–(c) Pressure distribution with different dimensionless sliding velocities $\frac{v\tau}{a_0} = 0.4, 0.8, 1.2$, respectively, and (d) evolution of the apparent friction coefficient μ_{app} with time at different sliding velocities.

Good agreement can be found between the simulation results derived from our model and the referred data from Koumi et al. [28], as shown in Figs. 4(a)–4(d).

As mentioned in Section 2.2, sliding motion is simulated by updating the coordinate of the contacting surface at any time point in the model. Some of the past pressure histories could be lost as a computational domain with a fixed size is applied during the simulation, where the pixel width is related to the sliding distance per time step. It is possible to keep the whole past pressure history in the record by extending the computational domain, but such an operation will impose a certain computational burden. To investigate the effect of the lost past pressure information on the sliding contact solution and to identify if it would become one of the limitations of our model, the following test, where two different numbers of nodes in x/y direction (denoted as L)

were applied in a frictionless sliding contact simulation with the velocity of $0.8a_0/\tau$, was conducted. The computational domain is set to be $-2.56a_0 \times 2.56a_0$ for the case with 256×256 nodes ($L = 256$) while it is increased to $-5.12a_0 \times 5.12a_0$ for the case with 512×512 nodes ($L = 512$).

As shown in Fig. 5(a), some of the past pressure histories are lost at several time points, including $0.0\tau, 0.5\tau, 1.0\tau$, when 256×256 nodes are applied. On the other hand, past pressure information is recorded completely when 512×512 nodes are applied as illustrated in Fig. 5(b). Contact solutions of the two cases (solid line for $L = 256$ and scatter for $L = 512$) are given in Fig. 5(c). The two curves of contact pressure fit perfectly initially while some insignificant difference appears at the final time point ($t = 3.975\tau$) as presented in the zoomed-in view in Fig. 5(c). The globally good agreement between the simulation results with different numbers of nodes indicates

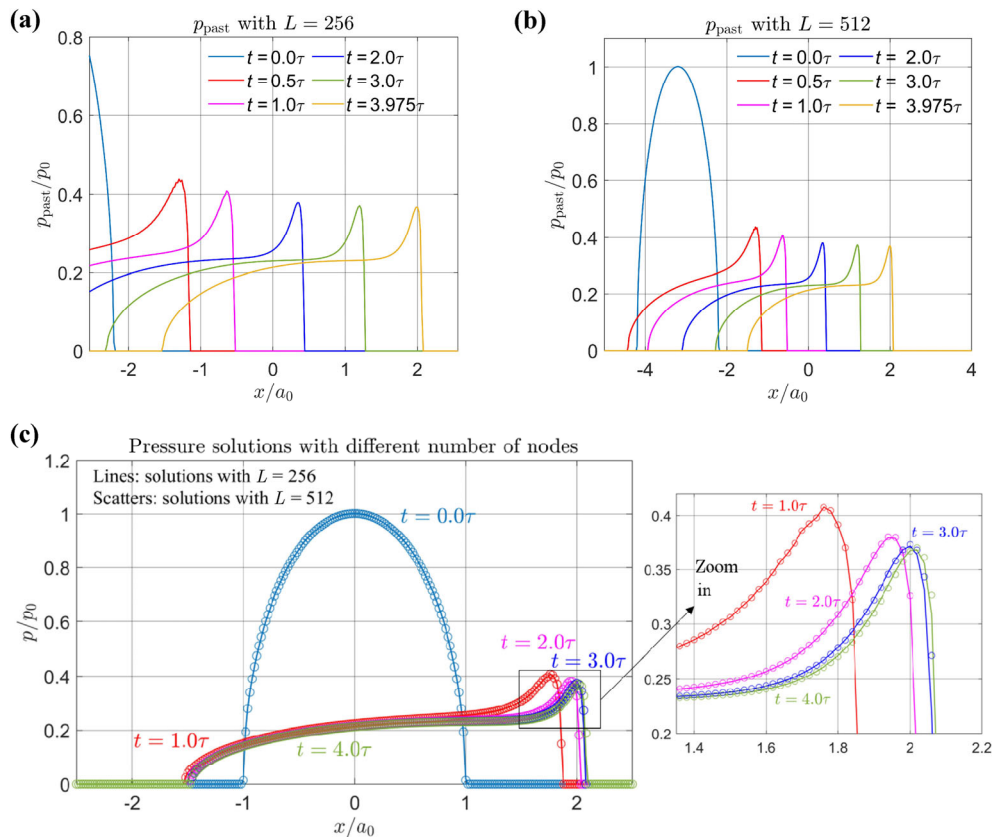


Fig. 5 Simulation results with different numbers of nodes L . (a) and (b) Past pressure history at the updated coordinates within $T = 4\tau$ with $L = 256$ and $L = 512$, respectively, and (c) comparison of contact pressures at different times for the two cases with $L = 256$ and $L = 512$, respectively.

that the lost past pressure information has micro effects on the contact solutions. Therefore, results derived from our model are reliable if an appropriate computational domain is specified to capture the creep of viscoelastic surfaces.

4 Results and discussion

Before moving to the frictional sliding contact modelling, it is noted that in our previous study on viscoelastic contacts [36], the parameter known as the ratio of retardation time to relaxation time (μ_∞ / μ_0) is found to determine the rheological behaviour of viscoelastic materials characterized by Zener models. Although the boundary value is yet unknown, materials with higher ratios tend to behave more fluid-like while those with lower ratios exhibit a more solid-like contact response. As a follow-up study, here the dependence of the pressure distribution and apparent friction coefficient on the rheology of

viscoelastic materials is first investigated.

4.1 Contact solutions in frictionless sliding and the effects of rheological properties

The frictionless sliding contacts of three different viscoelastic materials characterized by Zener models are simulated here. It is of note that contact solutions can be different depending on whether the contact is generated via a prescribed displacement or a fixed load since they represent distinct contact phenomena for viscoelastic materials. To describe it briefly, a creep phenomenon is encountered under a fixed normal load, where the contacting area keeps increasing with time. On the other hand, a stress relaxation phenomenon is encountered under a fixed normal displacement, where the contacting area remains while the normal pressure relaxes (decreases) with time. To complicate the study on the effects of rheological properties of viscoelastic materials on the sliding solutions, two different contact phenomena encountered in the normal

direction are tested by varying the contact input (constant load or displacement) to investigate their effects on sliding solutions. The detailed contact inputs specified in the tests are given in Table 2. The computational domain is set to be $-2.56a_0 \times 2.56a_0$ for all the tests, which is discretized by 256×256 nodes ($L = 256$).

As shown in Figs. 6(a)–6(c), when a stress relaxation phenomenon is experienced in the normal direction, the rear part of the contact region keeps shrinking with time. The shrink of contact area and relaxation of pressure becomes more significant for the more fluid-like material (e.g., the material with the higher value of μ_∞ / μ_0). For the more solid-like material ($\frac{\mu_\infty}{\mu_0} = 3$), the pressure profile is skewed less significantly compared with that of the more fluid-like material ($\frac{\mu_\infty}{\mu_0} = 10$). Besides, it seems to take more time for the frictionless viscoelastic contact to reach the steady state for the more solid-like material. This can be related to the relaxation modulus functions of the materials as shown in Fig. 6(d) such that the modulus of the more fluid-like material can reach a steady value within a shorter time.

To switch to the load-controlled case, the more fluid-like material (the material with a higher value of μ_∞ / μ_0) is found to exhibit a more significant creep phenomenon as shown in Figs. 7(a)–7(c). Similar to the displacement-controlled case, the pressure

profile is skewed more significantly for the more fluid-like material such that the peak pressure tends to appear on the rear edge of contacting area. However, the more fluid-like material tends to require more time to reach its steady contact state in the current creep case, which is related to the creep compliance of tested materials shown in Fig. 7(d). These simulation results are consistent with the finding of Zhao et al. [25], who reported the effects of a similar material parameter, which is known as the elasticity ratio in their study, on the steady-state pressure distribution when a creep phenomenon is encountered in the normal direction.

Regarding the pressure spikes in the pressure profile, the reason behind their occurrence shall be highlighted here. In our previous viscoelastic study regarding the effects of the rheological behaviour of materials on the shape of pressure in a normal indentation problem [36], the pressure spikes on both contacting edges can only be observed for the more fluid-like material for a certain time while the more solid-like always exhibits a Hertzian-type pressure distribution. The role played by the viscosity of viscoelastic materials determines the shape of the pressure profile in indentation problems. In this case, the viscosity of the more solid-like viscoelastic material has relatively trivial effects, where the contact behaviour is similar to that of elastic materials. Regarding the fluid-like material, its mechanical response could be first assumed as a pack of liquid being squeezed, where the indentation load keeps being distributed to the contacting edges. However, the material is not a real fluid after all. Eventually, it will reach a steady state, where elasticity plays a dominant role instead of viscosity and leads to a Hertzian-type pressure profile. For the sliding problem investigated here, it is the synergistic effect of sliding motion and viscosity of material (e.g., the friction derived from viscoelasticity during sliding) that leads to the commonly observed asymmetric pressure distribution. According to the studies in Refs. [19] and [25], the pressure profile becomes symmetric at considerably low or extremely high sliding speeds.

In terms of the frictional behaviour exhibited by different viscoelastic materials, as shown in Fig. 8, the more fluid-like material always shows a higher apparent friction coefficient regardless of the time and

Table 2 Contact parameters employed in the frictionless sliding test of different viscoelastic materials.

Parameter	Value	Description (unit)
W	1.50	Input indentation load (N)
δ	100	Input normal displacement (μm)
R	10	Radius of the sphere (mm)
μ_∞	3.86	Initial shear modulus of material (MPa)
$\frac{\mu_\infty}{\mu_0}$	3, 5, 10	Ratio of retardation time to relaxation time (ratio of initial shear modulus to modulus after infinite time)
τ	0.01	Relaxation time of the viscoelastic material (s)
ν	0.3	Poisson's ratio of the viscoelastic material
v	$0.8a_0 / \tau$	Frictionless sliding speed of the surface (normalized)

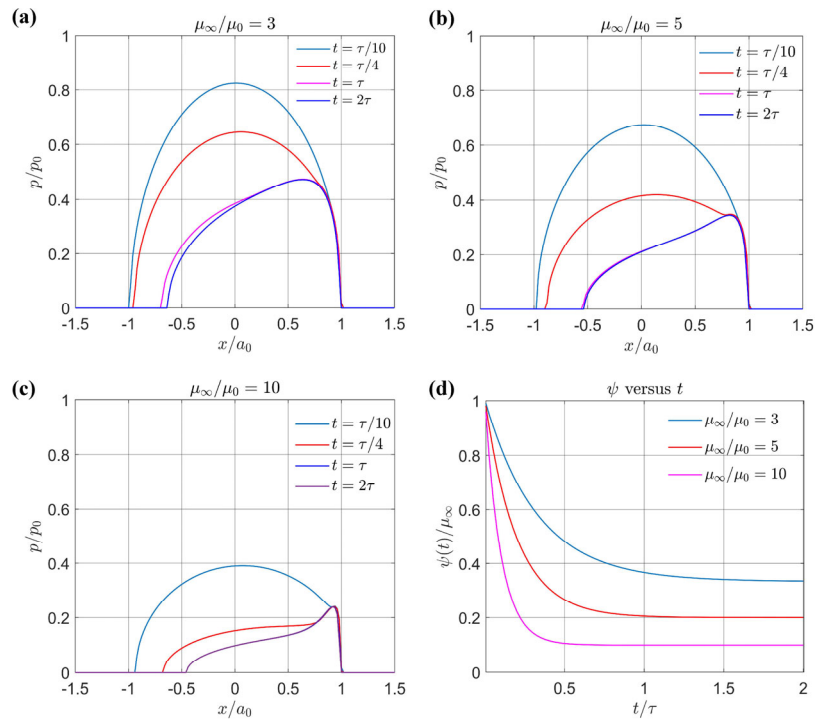


Fig. 6 Results of tested frictionless sliding contact problems under a constant displacement. (a)–(c) Pressure distributions of different materials characterised by Zener models $\frac{\mu_\infty}{\mu_0} = 3, 5, 10$, respectively, and (d) variations of relaxation modulus function with time for different materials.

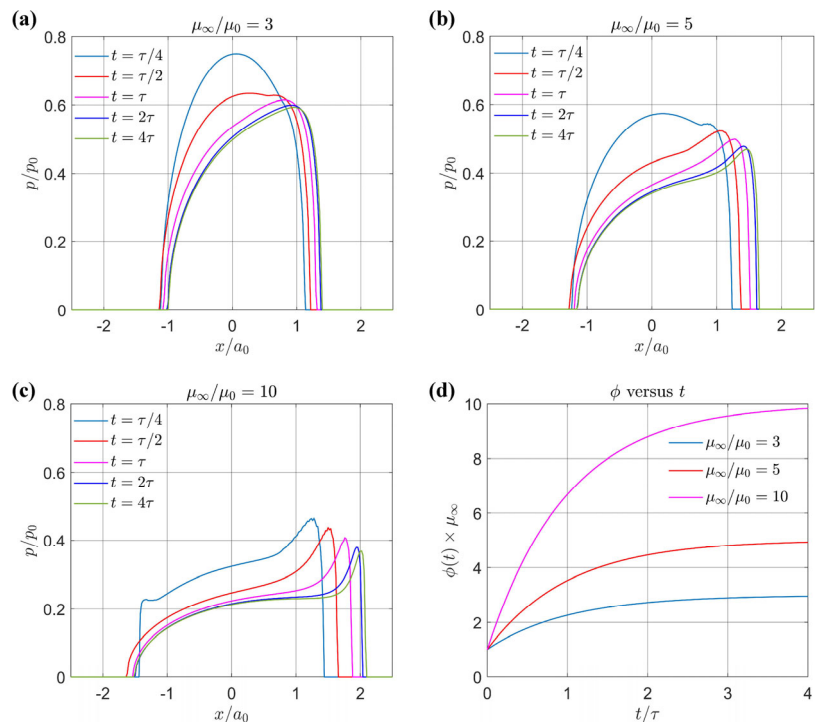


Fig. 7 Results of tested frictionless sliding contact problems under a constant load. (a)–(c) Pressure distributions of different viscoelastic materials characterised by Zener models $\frac{\mu_\infty}{\mu_0} = 3, 5, 10$, respectively, and (d) variation of creep compliance with time for different materials

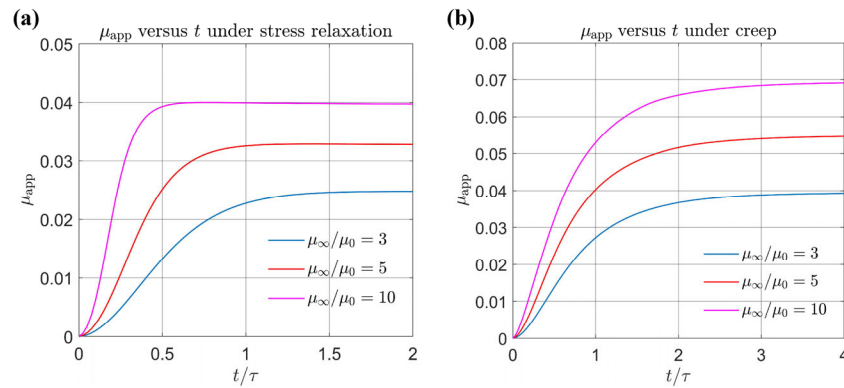


Fig. 8 Response of apparent friction coefficient with time for tested viscoelastic materials under different contact phenomena. (a) Stress relaxation and (b) creep.

the experienced contact phenomenon. This results from the more significant viscoelastic loss related to the dominant role played by the viscosity of the material. Compared with solutions under stress relaxation shown in Fig. 8(a), the apparent friction coefficient is always higher when the creep phenomenon is experienced by the same viscoelastic material as shown in Fig. 8(b). This suggests that a material can exhibit different levels of viscoelastic friction depending on whether the contact is generated by a specified penetration or load (experienced contact phenomenon).

4.2 Effects of partial slip period on the sliding solutions

To show the effects of the partial slip period, here four different cases of viscoelastic sliding are tested when a fixed displacement is specified in the normal direction. The first is the already conducted frictionless test. The second case is a frictional sliding test but without the initial partial slip period. In other words, the contact starts with gross slip and the effects of shear traction on the pressure profile are taken into account in this case, where the magnitude of shear traction is always equal to the local friction. The third case includes the partial slip period in the frictional sliding contact, where the gross slip happens before the material property reaches its steady state (gross sliding achieved at 0.1τ). The case where the gross slip happens relatively late (gross sliding achieved at 0.6τ , when the time-dependent material property becomes stable) is considered in the final test.

By specifying different linearly increasing rates of tangential displacement in x direction Δ_x in our

displacement-controlled algorithm (e.g., the increasing displacement is the model input while the increasing load is the output), the occurrences of gross sliding at different times for cases 3 and 4 are achieved. Once the gross sliding state is reached for the viscoelastic contact, the same sliding velocity v is specified for all four cases. The difference between static friction and dynamic friction is neglected here since a unified coefficient of friction is intended to be applied to simplify the frictional sliding simulations. The detailed contact inputs used in the tests are given in Table 3. The computational domain is set to be $-3.07a_0 \times 3.07a_0$

Table 3 Contact parameters employed in the frictional viscoelastic sliding test.

Parameter	Value	Description (unit)
δ_z	34.45	Input normal displacement (μm)
R	10	Radius of the sphere (mm)
μ_{∞}	3.86	Initial shear modulus of material (MPa)
μ_{∞} / μ_0	10	Ratio of retardation time to relaxation time (ratio of initial shear modulus to modulus after infinite time)
τ	0.01	Relaxation time of the viscoelastic material (s)
ν	0.3	Poisson's ratio of the viscoelastic material
μ_f	0.3	Coefficient of dry contact friction
$\Delta\delta_x$	$\frac{0.017a_0}{\tau}$, $\frac{0.17a_0}{\tau}$	Increment of tangential displacement per time step
v	$1.2a_0 / \tau$	Constant sliding speed of the viscoelastic surface (normalized) when the surface is in the gross sliding state

for all the cases, which is discretized by 256×256 nodes ($L = 256$).

The contact solutions of the four cases when the contact just initializes ($t = 0.0\tau$) are shown in Fig. 9(a). Due to the presence of shear tractions, cases 2, 3 and 4 exhibit different pressure profiles as illustrated in Fig. 9(a), right. The shear traction q_x is equal to the static friction (μp) for case 2 while cases 3 and 4 experience the same partial slip state exhibiting identical distributions of pressure and shear tractions as shown in Fig. 9(a), left. Compared with the two cases without a partial slip period, cases 3 and 4 show higher peak pressures at this moment.

For the next investigated time interval ($t = 0.1\tau$), the gross sliding is just reached for case 3 as indicated in Fig. 9(b), left, where the curve of shear traction agrees with that of static friction. The difference between the pressure profiles of cases 1 and 2 exists but it is still not significant at this time point as shown in Fig. 9(b), right. The shift of the contacting area in the direction of the sliding motion can be observed for these two cases while the contacting region tends to remain for cases 3 and 4 due to the mainly experienced stress relaxation phenomena in static states. Since case 4 is still in the partial slip period at $t = 0.1\tau$ as demonstrated in Fig. 9(b), left, the pressure profiles

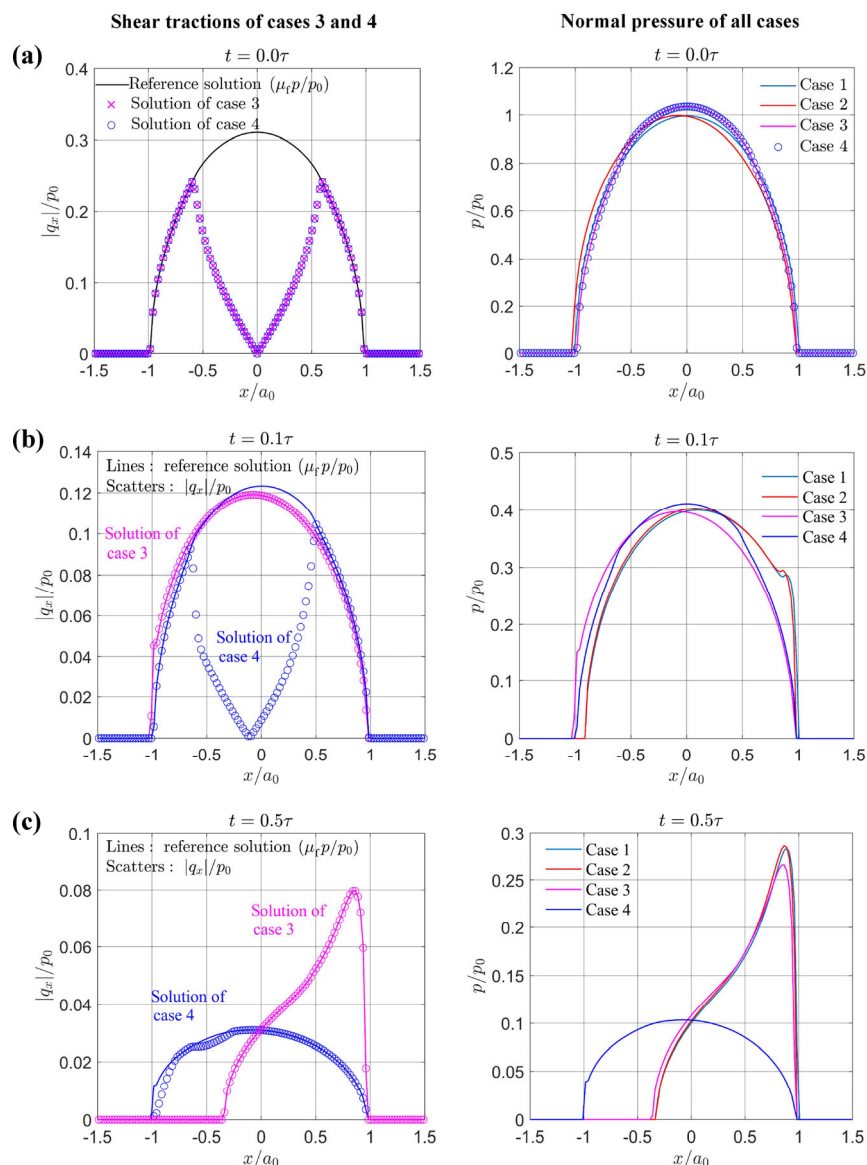


Fig. 9 Nondimensionalized contact solutions including the shear tractions of cases 3 and 4 (left) and normal pressures of four different cases (right) at different time. (a) $t = 0.0\tau$, (b) $t = 0.1\tau$, (c) $t = 0.5\tau$, (d) $t = 1.0\tau$, and (e) $t = 1.5\tau$.

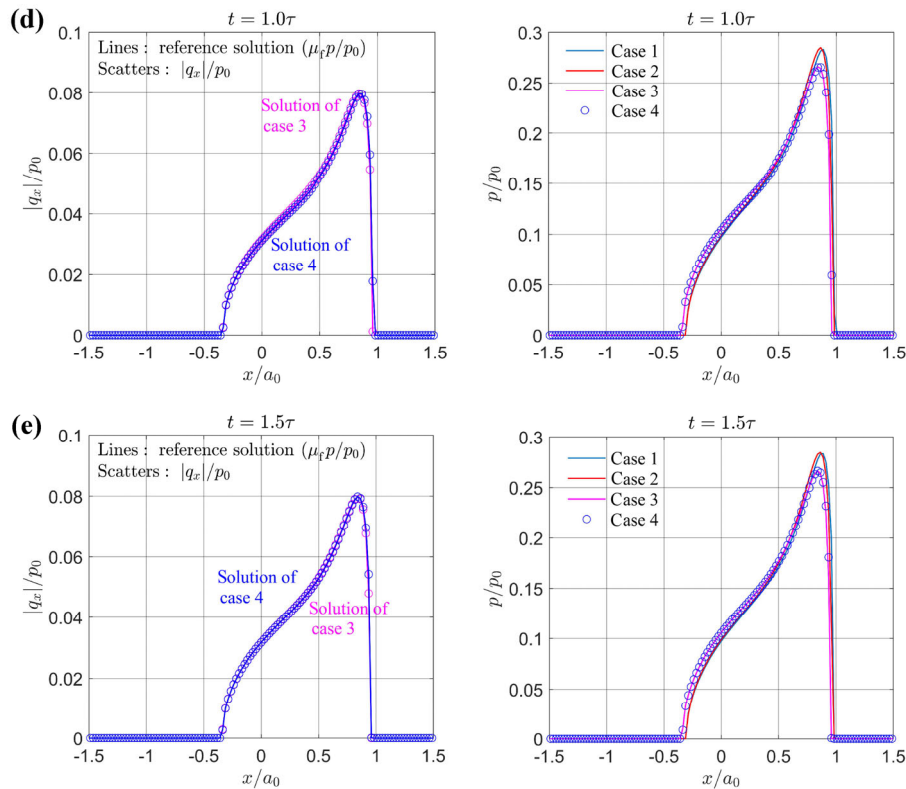


Fig. 9 (Continued)

of cases 3 and 4 are distinct currently.

For the time interval when the material property becomes stable and the frictionless sliding solution becomes steady ($t = 0.5\tau$), since case 4 has yet not reached the gross sliding region as indicated in Fig. 9(c), left, its pressure distribution is significantly different from the other cases as shown in Fig. 9(c), right. Due to the viscoelastic sliding motion, contact areas of surfaces in cases 1, 2, and 3 have shrunk, which leads to significantly higher peak pressures compared with the solution of case 4. Besides, after being in gross sliding for a certain time, the contact area of case 3 is found to shift in the same way as cases 1 and 2. However, this case now shows a lower peak pressure compared with the two cases without a partial slip period.

Contact solutions of another later time point ($t = 1.0\tau$) are given in Fig. 9(d), where the surface in case 4 has already been in a global slip state for a certain time as indicated in Fig. 9(d), left. Eventually, the shift of the shrinking contacting area is observed for case 4. Besides, the pressure solutions of other cases seem to reach a steady state as the difference can hardly be

found between Fig. 9(c), right and Fig. 9(d), right for cases 1, 2, and 3.

By extending the simulation time to 1.5τ , the contact becomes steadier for case 4 as the viscoelastic surface has been in the gross sliding state for a longer time as illustrated in Fig. 9(e), left. The overlap of pressure distribution curves is found for cases 3 and 4 as shown in Fig. 9(e), right. This suggests that the same pressure profile can be obtained by extending the simulation time to the steady contact state no matter when the partial slip period ends in a frictional sliding problem.

Cases including the partial slip period show a minor variation with the frictionless sliding solution regarding the shape of pressure distribution when the contact becomes steady. When the contact is in the steady regime, a slight difference can be observed when comparing the pressure magnitude as a lower peak pressure is observed for the case where partial slip has been experienced. Besides, the contacting region is slightly shifted in the direction opposite to the sliding motion for those cases. The difference between the solutions of frictional sliding contact

without partial slip period and frictionless sliding contact is relatively micro regardless of the time being referred to.

To switch the contact input in the normal direction to be a fixed load ($W = 0.15 \text{ N}$), since the time when the gross sliding happens barely causes any difference as long as the viscoelastic sliding contact reaches the steady state, only one frictional sliding contact with the presence of partial slip under creep input was tested with $\Delta\delta_x = 0.17a_0/\tau$. It was named case 3

while cases 1 and 2 stand for the frictionless test and frictional test without partial slip respectively. To take into account the creep of the contacting area under a constant normal load, the computational domain is increased to $-3.84a_0 \times 3.84a_0$ for the following tests.

The time-dependent contact solutions under the input of constant normal load are shown in Fig. 10. Like the above relaxation tests, when the contact initializes ($t = 0.0\tau$), due to the addition of dry contact friction in cases 2 and 3 and the resulting partial slip

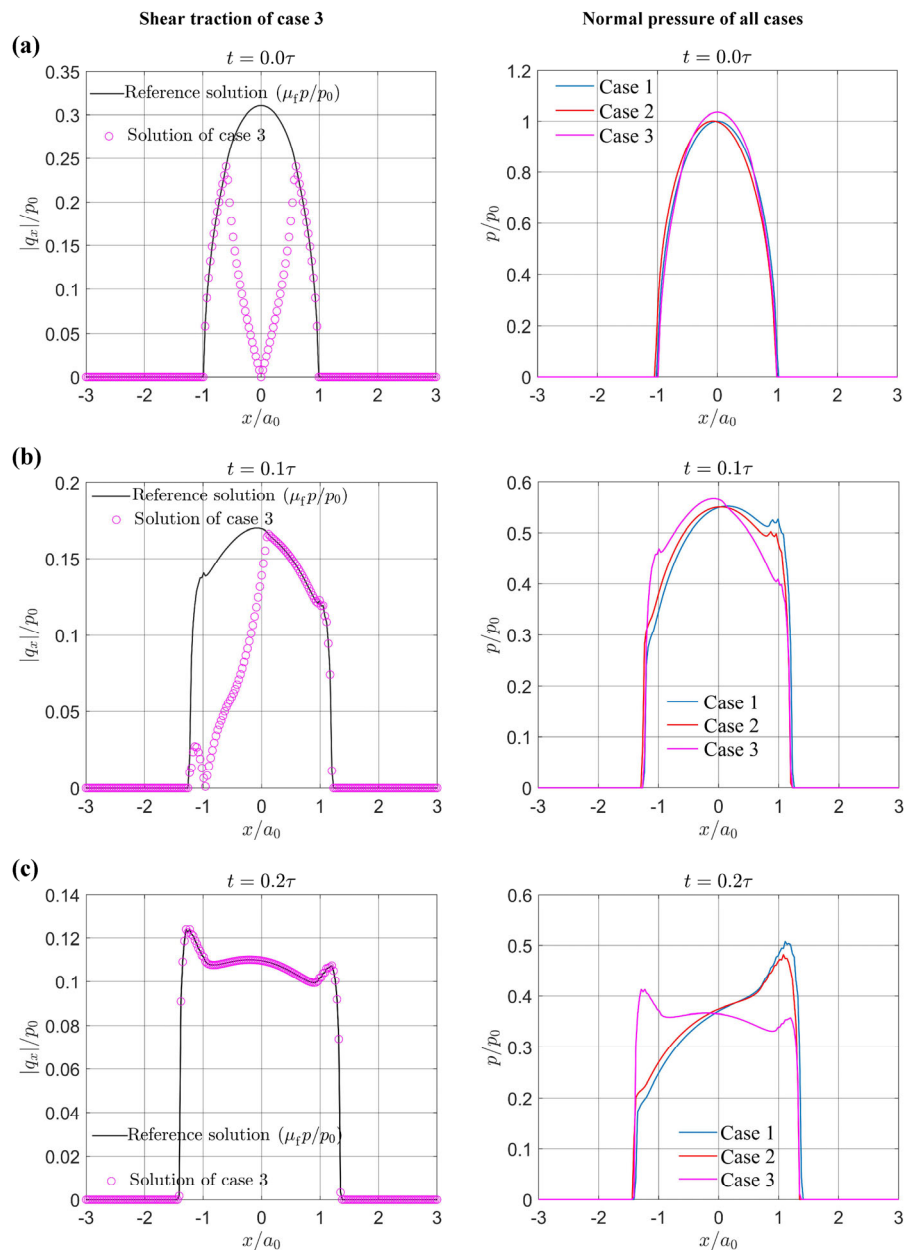


Fig. 10 Nondimensionalized solutions including the shear tractions of case 3 (left) and normal pressures of the three different cases (right) at different time points. (a) $t = 0.0\tau$, (b) $t = 0.1\tau$, (c) $t = 0.2\tau$, (d) $t = 1.0\tau$, and (e) $t = 4.0\tau$.

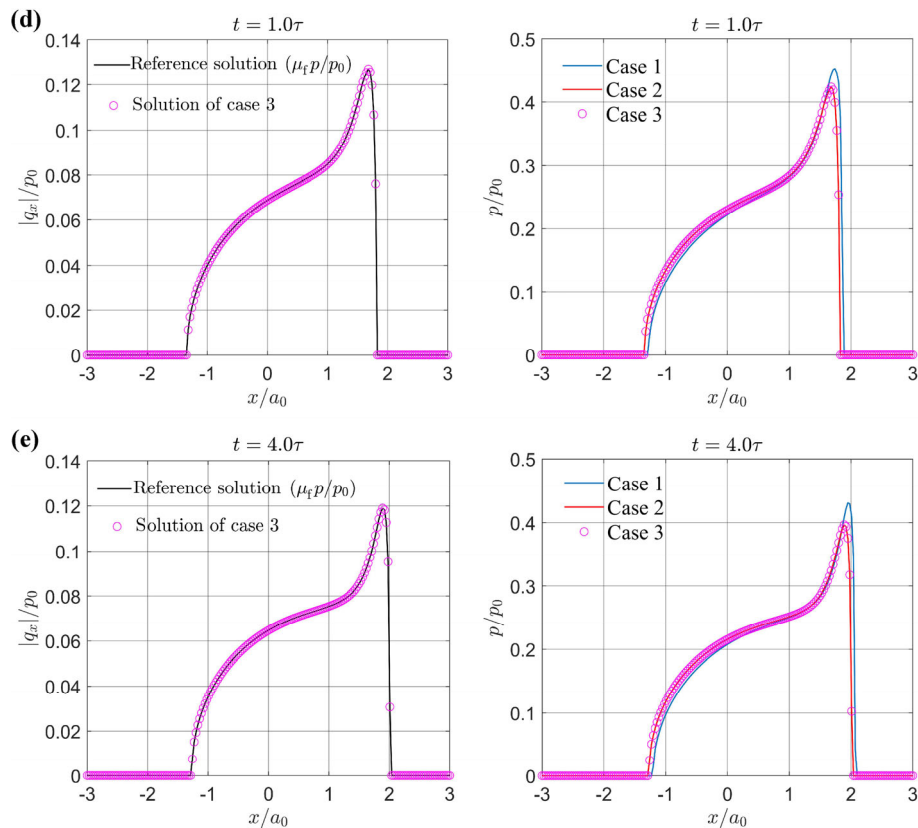


Fig. 10 (Continued)

phenomenon in case 3 shown in Fig. 10(a), left, the three cases exhibit different pressure profiles as shown in Fig. 10(a), right.

For the following two time points including $t = 0.1\tau$ and $t = 0.2\tau$, the viscoelastic surface in case 3 is found to experience a partial slip state as shown in Fig. 10(b), left and a gross slip state that is just achieved as illustrated in Fig. 10(c), left, respectively. Hence, the pressure profiles of case 3 are significantly different from the other two fully-slip cases at these two time points as shown in Fig. 10(b), right and Fig. 10(c), right, respectively.

Similar to the finding in our former study about viscoelastic indentation problems [36], fluctuating results are observed on the contact solutions for all the cases in Figs. 10(b) and 10(c). Although such oscillations could be alleviated by adopting a smaller time interval, the computational domain must be increased to characterize the creep of the contacting area as the pixel width of the mesh system is determined by the sliding distance during each time interval.

For the rest investigated time points ($t = 1.0\tau$ and $t = 4.0\tau$) when the viscoelastic surface in case 3 is in the gross slip state after certain times as illustrated in Fig. 10(d), left and Fig. 10(e), left, respectively, the pressure profiles of case 3 tend to become closer to those of case 2 as shown in Fig. 10(d), right and Fig. 10(e), right, respectively. What is different from the former relaxation test is that the load in the current creep test does not relax with time. Besides, different from the relaxation test where the contacting area of the sliding surface starts to shrink while that of the surface in the partial slip state remains, the contacting areas of the three cases almost remain identical regardless of the sliding states that are experienced by the viscoelastic surface at any time point as illustrated in Fig. 10. Together with the fact that viscoelastic surface exhibits different frictional resistance to sliding depending on whether the stress relaxation or creep phenomenon is experienced in the normal direction, the partial slip regime has different effects on the later sliding solutions as discussed. However, as shown in Figs. 9 and 10, the differences

between the pressure profiles of all the tested cases are not significant but yet exist when the contacting viscoelastic surface is at a steady state.

5 Conclusions

The sliding aspect of the developed model is validated against the simulation results of Koumi et al. [28] for a spherical frictionless sliding contact problem. The dependence of the distribution of contact pressure and dissipative losses on the rheological property of viscoelastic materials is analysed based on the developed sliding contact model for viscoelastic materials. It was found that the more fluid-like viscoelastic material, for which the pressure profile is skewed more remarkably, exhibits higher frictional resistance to sliding motion due to the more dissipative loss arising from the dominant role of its viscosity. As a result, the shrinkage of contacting area for the more fluid-like viscoelastic material is more significant when the stress relaxation phenomenon is experienced in the normal direction.

The frictional viscoelastic sliding contact with the partial slip period is analysed in this paper. Beyond the fact that the partial slip regime caused a micro change in the normal pressure distribution when the contact becomes steady, it delays the time required by the viscoelastic sliding surface to reach its steady state. This suggests that the assumption of frictionless contact (no dry friction), which is adopted in most numerical and theoretical models, could induce quantitative differences when analysing the sliding contact of viscoelastic materials. Qualitative errors may even be encountered when the observation time is too small to capture the actual steady state of the contacting surfaces. We believe that our numerical study can serve as a good reference for the future modelling work about the sliding contact of viscoelastic materials. If the steady-state solution is the primary concern and of greater interest for researchers, they can simplify the contact problem under consideration (i.e., neglect the dry contact friction and conduct a frictionless sliding contact analysis instead) to obtain qualitative-correct results. However, in some cases such as a contact system subjected to dynamic loading, it is necessary to perform transient contact

analysis on the sliding viscoelastic materials, where the role played by dry friction should be considered. Understanding the contact traction history during the evolution period from partial slip to gross sliding and pinpointing the time at which gross sliding begins can lead to a quantitatively-correct contact analysis. This, in turn, enhances our grasp of friction and wear of materials and improves our ability to predict material performance.

Considering that the contact solutions presented in the study are limited to the half-space approximation while viscoelastic materials often exist in the form of a layer with a finite thickness in practice, the development of a model for the sliding contact of viscoelastic layers is necessary. This is the subject of our current ongoing work.

Apart from the single-asperity contact considered in the study, the transient multi-asperity (rough-surface) contact needs to be investigated numerically to shed light on the role played by the surface roughness in frictional sliding contact solutions of viscoelastic materials. Furthermore, the assumption of no adhesive force might undermine the validity of the simulation results especially when the viscoelastic material is significantly softer or more compliant than the other contacting materials. A model, which integrates the effects of adhesive force and viscoelasticity, shall provide a more helpful contact analysis of viscoelastic materials. These are knowledge gaps that currently exist and need to be filled in the future.

Acknowledgements

The authors are thankful to the School of Mechanical Engineering at the University of Leeds for supporting this study by funding the Ph.D. studentship of Dongze WANG. This work is supported by the Engineering and Physical Sciences Research Council (Grant No. EP/T024542/1) as part of ‘STOP fibrous microplastic pollution from textiles by elucidating fibre damage and manufacturing novel textiles’ standard research.

Declaration of competing interest

The authors have no competing interests to declare that are relevant to the content of this article.

Open Access This article is licensed under a Creative Commons Attribution 4.0 International License, which permits use, sharing, adaptation, distribution and reproduction in any medium or format, as long as you give appropriate credit to the original author(s) and the source, provide a link to the Creative Commons licence, and indicate if changes were made.

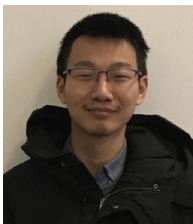
The images or other third party material in this article are included in the article's Creative Commons licence, unless indicated otherwise in a credit line to the material. If material is not included in the article's Creative Commons licence and your intended use is not permitted by statutory regulation or exceeds the permitted use, you will need to obtain permission directly from the copyright holder.

To view a copy of this licence, visit <http://creativecommons.org/licenses/by/4.0/>.

References

- [1] Persson B N J. Rubber friction and tire dynamics. *J Phys: Condens Matter* **23**: 015003 (2010)
- [2] Cheng Q Q, Liu P X, Lai P H, Zou Y N. An interactive meshless cutting model for nonlinear viscoelastic soft tissue in surgical simulators. *IEEE Access* **5**: 16359–16371 (2017)
- [3] Lawless B M, Sadeghi H, Temple D K, Dhaliwal H, Espino D M, Hukins D W L. Viscoelasticity of articular cartilage: Analysing the effect of induced stress and the restraint of bone in a dynamic environment. *J Mech Behav Biomed Mater* **75**: 293–301 (2017)
- [4] Lu X, Meng Q, Wang J, Jin Z. Transient viscoelastic lubrication analyses of UHMWPE hip replacements. *Tribol Int* **128**: 271–278 (2018)
- [5] Kiumarsi M, Rafe A, Yeganehzad S. Effect of different bulk sweeteners on the dynamic oscillatory and shear rheology of chocolate. *Appl Rheol* **27**: 11–19 (2017)
- [6] Van Dokkum J S, Nicola L. Green's function molecular dynamics including viscoelasticity. *Modell Simul Mater Sci Eng* **27**: 075006 (2019)
- [7] Hunter S C. The rolling contact of a rigid cylinder with a viscoelastic half space. *J Appl Mech* **28**: 611–617 (1961)
- [8] Panek C, Kalker J J. Three-dimensional contact of a rigid roller traversing a viscoelastic half space. *IMA J Appl Math* **26**: 299–313 (1980)
- [9] Goriacheva I G. Contact problem of rolling of a viscoelastic cylinder on a base of the same material. *J Appl Math Mech* **37**: 877–885 (1973)
- [10] Aleksandrov V M, Goryacheva I G, Torskaya E V. Sliding contact of a smooth indenter and a viscoelastic half-space (3D problem). *Dokl Phys* **55**: 77–80 (2010)
- [11] Persson B N J. Rolling friction for hard cylinder and sphere on viscoelastic solid. *Eur Phys J E* **33**: 327–333 (2010)
- [12] Wang D, de Boer G, Neville A, Ghanbarzadeh A. A review on modelling of viscoelastic contact problems. *Lubricants* **10**: 358 (2022)
- [13] Padovan J, Paramadilok O. Transient and steady state viscoelastic rolling contact. *Comput Struct* **20**: 545–553 (1985)
- [14] Padovan J, Kazempour A, Tabaddor F, Brockman B. Alternative formulations of rolling contact problems. *Finite Elem Anal Des* **11**: 275–284 (1992)
- [15] Le Tallec P, Rahler C. Numerical models of steady rolling for non-linear viscoelastic structures in finite deformations. *Int J Numer Meth Eng* **37**: 1159–1186 (1994)
- [16] Nackenhorst U. The ALE-formulation of bodies in rolling contact: Theoretical foundations and finite element approach. *Comput Method Appl M* **193**: 4299–4322 (2004)
- [17] Padovan J. Finite element analysis of steady and transiently moving/rolling nonlinear viscoelastic structure—I. Theory. *Comput Struct* **27**: 249–257 (1987)
- [18] Nasdala L, Kaliske M, Becker A, Rothert H. An efficient viscoelastic formulation for steady-state rolling structures. *Comput Mech* **22**: 395–403 (1998)
- [19] Carbone G, Putignano C. A novel methodology to predict sliding and rolling friction of viscoelastic materials: Theory and experiments. *J Mech Phys Solids* **61**: 1822–1834 (2013)
- [20] Carbone G, Putignano C. Rough viscoelastic sliding contact: Theory and experiments. *Phys Rev E* **89**: 032408 (2014)
- [21] Menga N, Putignano C, Carbone G, Demelio G P. The sliding contact of a rigid wavy surface with a viscoelastic half-space. *Proc R Soc A* **470**: 20140392 (2014)
- [22] Putignano C, Carbone G, Dini D. Mechanics of rough contacts in elastic and viscoelastic thin layers. *Int J Solids Struct* **69–70**: 507–517 (2015)
- [23] Menga N, Afferrante L, Carbone G. Effect of thickness and boundary conditions on the behavior of viscoelastic layers in sliding contact with wavy profiles. *J Mech Phys Solids* **95**: 517–529 (2016)
- [24] Menga N, Afferrante L, Demelio G P, Carbone G. Rough contact of sliding viscoelastic layers: Numerical calculations and theoretical predictions. *Tribol Int* **122**: 67–75 (2018)
- [25] Zhao Y, Morales-Espejel G E, Venner C H. Aspects of modeling and numerical simulation of dry point contacts

- between viscoelastic solids. *Tribol Int* **165**: 107245 (2022)
- [26] Venner C H, Lubrecht A A. *Multilevel Methods in Lubrication*. Amsterdam (NL): Elsevier Science, 2000.
- [27] Brandt A, Lubrecht A A. Multilevel matrix multiplication and fast solution of integral equations. *J Comput Phys* **90**: 348–370 (1990)
- [28] Koumi K E, Chaise T, Nelias D. Rolling contact of a rigid sphere/sliding of a spherical indenter upon a viscoelastic half-space containing an ellipsoidal inhomogeneity. *J Mech Phys Solids* **80**: 1–25 (2015)
- [29] Bugnicourt R, Sainsot P, Lesaffre N, Lubrecht A A. Transient frictionless contact of a rough rigid surface on a viscoelastic half-space. *Tribol Int* **113**: 279–285 (2017)
- [30] Wallace E R, Chaise T, Nelias D. Three-dimensional rolling/sliding contact on a viscoelastic layered half-space. *J Mech Phys Solids* **143**: 104067 (2020)
- [31] Zhang X, Wang Q J, He T. Transient and steady-state viscoelastic contact responses of layer-substrate systems with interfacial imperfections. *J Mech Phys Solids* **145**: 104170 (2020)
- [32] Goryacheva I, Stepanov F, Torskaya E. Effect of friction in sliding contact of a sphere over a viscoelastic half-space. In: International Conference on Mathematical Modeling and Optimization in Mechanics, Jyväskylä, Finland, 2016: 93–103.
- [33] Goryacheva I G, Stepanov F I, Torskaya E V. Sliding of a smooth indenter over a viscoelastic half-space when there is friction. *J Appl Math Mech* **79**: 596–603 (2015)
- [34] Bugnicourt R. Simulation of the contact between a rough surface and a viscoelastic material with friction. Lyon (France): Université de Lyon, 2017.
- [35] Wayne Chen W, Jane Wang Q, Huan Z, Luo X. Semi-analytical viscoelastic contact modeling of polymer-based materials. *J Tribol* **133**: 1–10 (2011)
- [36] Wang D, de Boer G, Ghanbarzadeh A. A numerical model for investigating the effect of viscoelasticity on the partial slip solution. *Materials* **15**: 5182 (2022)
- [37] Yakovenko A, Goryacheva I. The periodic contact problem for spherical indenters and viscoelastic half-space. *Tribol Int* **161**: 107078 (2021)
- [38] Wang D, de Boer G, Neville A, Ghanbarzadeh A. A new numerical model for investigating the effect of surface roughness on the stick and slip of contacting surfaces with identical materials. *Tribol Int* **159**: 1–21 (2021)
- [39] Wang D, de Boer G, Nadimi S, Neville A, Ghanbarzadeh A. A fully coupled normal and tangential contact model to investigate the effect of surface roughness on the partial slip of dissimilar elastic materials. *Tribol Lett* **70**: 98 (2022)
- [40] Aili A, Vandamme M, Torrenti J M, Masson B. Theoretical and practical differences between creep and relaxation Poisson's ratios in linear viscoelasticity. *Mech Time-Depend Mater* **19**: 537–555 (2015)
- [41] Bonari J, Paggi M. Viscoelastic effects during tangential contact analyzed by a novel finite element approach with embedded interface profiles. *Lubricants* **8**: 107 (2020)
- [42] Boussinesq J. Applications des potentiels à l'étude de l'équilibre et mouvement des solides élastiques. *Gauthier-Villard, Paris* (1885).



Dongze WANG. He received his M.Sc. degree in mechanical engineering from University of Leeds, UK. He is currently pursuing a Ph.D. degree in mechanical engineering

at University of Leeds, under the supervision of Dr. Ali GHANBARZADEH and Dr. Gregory de BOER. His current scientific interests are numerical modelling, tribochemistry, and contact mechanics.



Greg de BOER. He received his Ph.D. in mechanical engineering from University of Leeds, UK, in 2015. He is currently a lecturer in

aeronautical and aerospace engineering. His current scientific interests are multiscale modelling of lubricated contacts, computational fluid mechanics, and compliant structural mechanics simulations.



Anne NEVILLE. She received her Ph.D. in mechanical engineering from University of Glasgow, UK,

in 1995. She was a professor leading the research work in the fields of tribology and corrosion at University of Leeds.



Ali GHANBARZADEH. He received his Ph.D. in mechanical engineering from University of Leeds, UK, in 2016. He is currently a lecturer in

functional surfaces. His current scientific interests are contact mechanics of rough surfaces, contact mechanics of rough surfaces and tribocorrosion.